

Effect of hydrogen on catalyst nanoparticles in carbon nanotube growth

Michael J. Behr, E. Ashley Gaulding, K. Andre Mkhoyan, and Eray S. Aydil^{a)}
Department of Chemical Engineering and Materials Science, University of Minnesota, Minneapolis, Minnesota 55455, USA

(Received 30 April 2010; accepted 30 June 2010; published online 13 September 2010)

The structures of carbon nanotubes grown from catalytic nanoparticles via plasma-enhanced chemical vapor deposition in CH₄/H₂ mixtures show a strong dependence on the H₂-to-CH₄ ratio in the feed gas. A suite of characterization techniques, including optical emission, infrared, and Raman spectroscopies combined with convergent-beam and selected-area electron diffraction, and high-resolution (scanning) transmission electron microscopy imaging were used to systematically investigate the interrelation among plasma gas phase composition, catalyst morphology, catalyst structure, and carbon nanotube structure. Hydrogen plays a critical role in determining the final carbon nanotube structure through its effect on the catalyst crystal structure and morphology. At low H₂-to-CH₄ ratios (~1), iron catalyst nanoparticles are converted to Fe₃C and well-graphitized nanotubes grow from elongated Fe₃C crystals. High (>5) H₂-to-CH₄ ratios in the feed gas result in high hydrogen concentrations in the plasma and strongly reducing conditions, which prevents conversion of Fe to Fe₃C. In the latter case, poorly-graphitized nanofibers grow from ductile bcc iron nanocrystals that are easily deformed into tapered nanocrystals that yield nanotubes with thick walls. © 2010 American Institute of Physics. [doi:10.1063/1.3467971]

I. INTRODUCTION

Carbon nanotubes (CNTs) exhibit a combination of unique thermal, optical, and electronic properties that make them desirable for a wide range of applications from transparent conducting films to sensors and transistors.¹ Many of these properties depend on how the carbon atoms are arranged within the graphene wall(s).^{2,3} Precise structural control of this arrangement remains the key challenge to realizing their technological potential.⁴ Plasma-enhanced chemical vapor deposition (PECVD) from methane-hydrogen or acetylene-hydrogen gas mixtures using catalytic iron nanoparticles enables large-scale growth of dense carbon nanotubes (CNTs). Hydrogen is required to grow well-graphitized CNTs,⁵ however, the structure of the nanotubes can vary significantly depending on how much hydrogen is present during growth. A number of research groups varied the fraction of hydrogen in the precursor gas mixture and reported changes in CNT size, structure, morphology, or areal nanotube density.⁵⁻¹² A general consensus is that hydrogen etches away any amorphous carbon that may deposit on the catalyst and block the nanotube growth.⁴ However, this mechanism alone does not explain the strong dependence of nanotube structure on hydrogen concentration. Another issue that has not yet been addressed systematically is the effect of hydrogen on the shape, structure, and composition of the catalyst particles. Indeed, CNTs and carbon nanofibers (CNFs) have been reported to grow by PECVD or CVD from a number of different catalyst morphologies,¹³ and catalyst phases, including pure iron and a variety of iron carbide phases, such as Fe₃C, Fe₅C₂, and Fe₇C₃.¹⁴⁻¹⁸ Nanotube structure appears to have some correlation to the shape and size of the catalyst.^{13,19} However, a thorough examination of catalyst

crystals as a function of hydrogen concentration in the plasma has not yet been reported. In this study, convergent beam electron diffraction (CBED) and high-resolution transmission electron microscopy (HR-TEM) and related techniques were used to explain the changes in catalyst crystal morphology, size, composition, and structure as a function of hydrogen concentration in the feed gas and in the plasma.

II. EXPERIMENTAL

Dense multiwall CNT (MWCNT) films were grown using a radio-frequency (rf at 13.56 MHz) inductively-coupled plasma and initially iron catalyst through PECVD. The iron catalyst was deposited on native-oxide coated silicon substrates as a 10 nm thick film using electron-beam evaporation. Substrates were placed on a resistively heated substrate platen located 25 cm below the transformer-coupled plasma coil, in a down-stream type configuration.²⁰ Before nanotube growth, the iron catalyst film was exposed to a H₂:Ar [50:5 SCCM (SCCM denotes cubic centimeter per minute at STP)] plasma (200 W rf power) at 700 °C for 15 min to break apart the film to form nanometer-size metal islands, and to reduce oxides present in the catalyst film. Growth of the nanotubes was conducted at 800 °C and 10 Torr using a plasma maintained with 200 W rf power in a CH₄:H₂:Ar gas mixture. In this study, the flow rate of hydrogen was varied from 0 to 100 SCCM, while the CH₄:Ar flow rate ratio remained fixed at 5:68 SCCM. Dihydrogen flow rates used in this study were 0, 5, 25, 50, and 100 SCCM, which correspond to H₂-to-CH₄ flow rate ratios of 0, 1, 5, 10, and 20, respectively.

Relative concentrations of H, CH, and C₂ species in the plasma were monitored using optical emission spectroscopy (OES) in conjunction with actinometry as described by Coburn and Chen.²¹ Argon was chosen as the actinometer; its flow remained constant at 68 SCCM for all experiments. All

^{a)}Electronic mail: aydil@umn.edu.

peak intensities in OES measurements were normalized relative to the Ar 750.4 nm emission line, to account for changes in the electron density and distribution of electron energies.^{21,22} Emission averaged over the entire plasma volume was coupled via a fiber-optic cable to an Acton Research Corporation SpectraPro-275 0.275 Meter Triple Grating Monochromator/Spectrograph equipped with a photomultiplier tube. Using a grating with 1200 grooves/mm combined with a 50 μm entrance slit width yielded 0.15 nm spectral resolution. All spectra were collected with a 0.1 nm scan step and 200 ms integration time. Emission intensities from species of interest were measured from peak heights.

Absorption by infrared active gas phase species was examined with and without plasma using Fourier transform infrared (FTIR) spectroscopy (Nicolet Magna-IR 550 FTIR spectrometer). Methane and acetylene could be detected using FTIR. Gas temperature and methane dissociation fraction in the plasma were calculated from measured infrared absorption spectra. The IR beam from the spectrometer was directed into the plasma reaction chamber through KBr windows. Total path length of the IR beam through the plasma was 54.5 cm. The transmitted beam was then detected with an external, cooled HgCdTe detector. Absorption spectra in the range of 650–4000 cm^{-1} with a spectral resolution of 0.5 cm^{-1} were averaged over 300 scans and recorded. The change in magnitude as well as the change in rotational-level population of the methane rotation-vibration absorption band, centered at 3017 cm^{-1} , was used to calculate the change in CH_4 density and gas rotational temperature, respectively. All spectra were collected relative to reference spectra with no gas flowing through the reaction chamber.

Average CNT structure was characterized using Raman spectroscopy. Raman spectra of the nanotube films were collected using a Witec alpha300R Raman spectrometer in the confocal backscattering geometry. An argon ion laser (514.5 nm wavelength) operating at 20 mW and focused to ~ 1 μm spot provided excitation. Raman scattering was detected using a DV401 charge coupled device (CCD) peltier-cooled detector.

Characterization of individual CNTs and catalysts, including high-resolution imaging combined with CBED and selected area electron diffraction (SAED), was conducted using an FEI Tecnai F-30 microscope with a Schottky field-emission electron gun operated at 300 kV. Nanotubes were removed from the Si/SiO₂ substrates by sonication in ethanol for 30 s, and then transferred to copper TEM grids coated with a lacey carbon support film. Images and diffraction patterns were recorded using a Gatan CCD.

III. RESULTS AND DISCUSSION

A. Gas phase analysis

Optical emission provided the relative concentrations of optically active reactive species in the plasma as a function of the dihydrogen concentration in the feed gas. In all experiments, emission from atomic H (H_α at 656 nm), CH (431 nm), C_2 (516 nm), and Ar (750.4 nm) was detected; these are commonly observed emission lines from plasmas containing Ar, CH_4 , and H_2 .²³ Using actinometry, changes to the relative

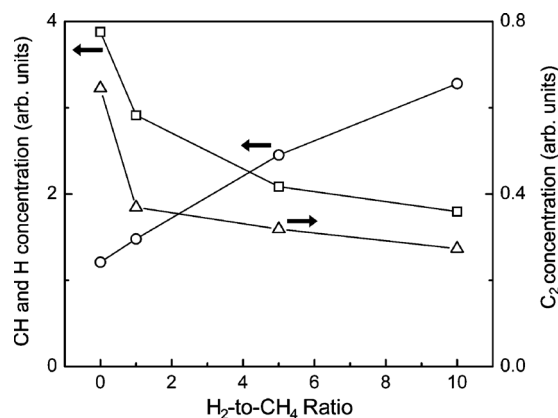


FIG. 1. Optical emission intensities of H_α (656 nm, \circ), CH (431 nm, \square), and C_2 (516 nm, \triangle) normalized with the Ar 750.4 nm emission intensity, and plotted as a function of H_2 -to- CH_4 flow rate ratio.

ground-state concentration of each species present under different hydrogen flows were determined. As an example, the relative ground-state H and Ar concentrations, $[\text{H}]/[\text{Ar}]$ can be related to their relative emission intensity ratio, I_{656}/I_{750} , through the relation $[\text{H}]/[\text{Ar}] = kI_{656}/I_{750}$, where k is the proportionality constant.²¹ Ma *et al.*²⁴ found very good agreement between relative specie concentrations in a microwave $\text{CH}_4/\text{Ar}/\text{H}_2$ plasma determined using actinometry and absolute densities measured with cavity ring-down spectroscopy. Figure 1 shows the relative ground-state concentrations of the H, CH, and C_2 , as a function of H_2 -to- CH_4 flow ratio. Relative H concentration is lowest in the pure methane plasma. Hydrogen atoms can be produced only from CH_4 under these conditions. As H_2 gas is added to the plasma, relative H concentration increases linearly. Over the range of H_2 -to- CH_4 ratios used in this study, the relative H atom concentration was found to vary by a factor of three. An opposite trend was observed for CH and C_2 species. Relative concentrations of these species are at a maximum in the pure methane plasma. With addition of only 5 SCCM of H_2 (equal to methane flow), their relative concentration in the plasma dropped significantly. At 25 SCCM H_2 , this ratio was approximately half that compared to the pure methane plasma. Further increase in H_2 , to ten times the amount of CH_4 , resulted in a smaller decrease in both CH and C_2 concentrations.

Figure 2(a) shows a typical IR rotation-vibration absorption band of gas-phase methane in the reaction chamber, centered at 3017 cm^{-1} . The black curve was obtained with the plasma off, while the red curve was measured after turning on the plasma at 200 W rf power. The gas temperature and the fraction of methane dissociated by the plasma were calculated from IR spectra. The population of rotational levels follows a Boltzmann distribution, and was used to calculate the rotational temperature of the gas molecules as shown in Fig. 2(b). Details of this calculation are presented in the Appendix. With the plasma off, the gas temperature was 300 K, while with the plasma on, the highest calculated rotational temperature was found to be 345 K. The rotational, translational, and vibrational temperatures are all approximately equal because of the high pressure (10 Torr) used in these experiments. With no significant change in gas temperature

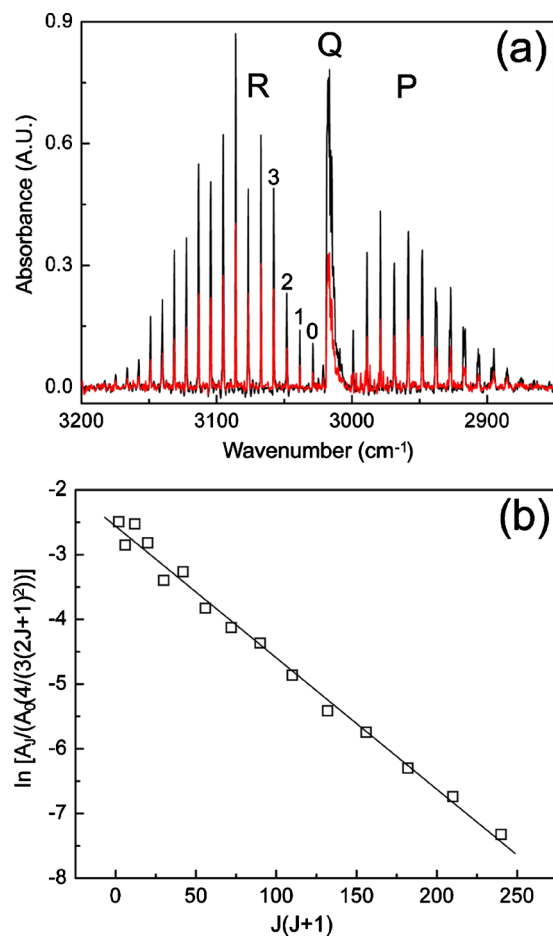


FIG. 2. (Color online) (a) Typical rotation-vibration IR absorption spectra of methane gas at 10 Torr with plasma on (red) and plasma off (black). The first few rotational peaks of the R branch are labeled with the appropriate angular momentum quantum number. (b) The intensities of rotational absorption peaks from the R branch are displayed on a Boltzmann plot. A linear fit yielded a slope inversely proportional to the gas temperature.

during plasma activation, the concentration of reactive species formed in the plasma through dissociation of methane or hydrogen could be determined from pressure measurements, as presented in the Appendix. Additionally, fraction of methane dissociation could be calculated from IR absorption measurements. The magnitude of the red absorption band is less than that of the black [see Fig. 2(a)] because a fraction of the methane molecules are dissociated in the plasma to form other species. This change in absorption is a direct measure of the fraction of methane dissociated in the plasma. Figure 3(a) shows the fraction of methane dissociated in the plasma as a function of the H₂-to-CH₄ flow rate ratio. This fraction ranges from 56% in the pure methane plasma, to only 21% when the H₂ flow rate is 50 SCCM (10 times the CH₄ flow rate). The absolute concentration of methane molecules as well as the concentration of methane molecules that are dissociated to form other reactive species, (e.g., C₂, C₂H₂, CH_x, etc.) in the plasma are also plotted in Fig. 3(a). Over the range investigated, it is found that increasing the amount of hydrogen in the gas mixture decreases the concentration of reactive species that are formed from the dissociation of methane by a factor of three.

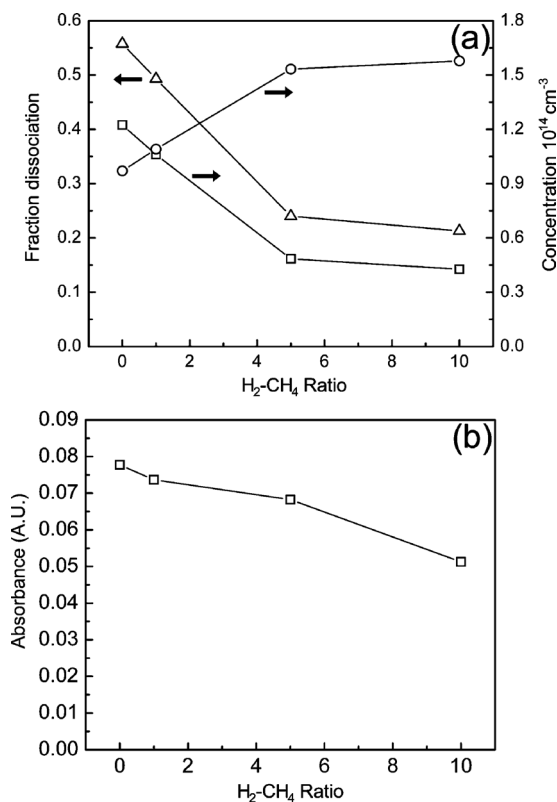


FIG. 3. (a) Fractional dissociation of CH₄ in the plasma (Δ), concentration of CH₄ that is not dissociated (○), and concentration of CH₄ that was dissociated in the plasma (□) as a function of H₂-to-CH₄ flow rate ratio. (b) Integrated intensity of acetylene absorption peak at 730 cm⁻¹ as a function of H₂-to-CH₄ flow rate ratio.

In addition to methane absorption bands, also present in spectra from all experiments with plasma activation were absorption bands corresponding to acetylene, C₂H₂, located at 3300 and 730 cm⁻¹.²⁵ The integrated intensity of the absorption band located at 730 cm⁻¹ is plotted as a function of H₂-to-CH₄ flow rate ratio in Fig. 3(b). Consistent with the other carbon-containing species formed in the plasma, i.e., CH and C₂, the concentration of C₂H₂ also decreases with increasing H₂ fraction. The decrease in acetylene concentration (~34%) over the range investigated is of similar magnitude to the observed change in fraction of methane dissociation (~35%).

In summary, gas phase characterization indicates that when the H₂-to-CH₄ ratio in the feed gas is increased from 0 to 10, concentration of H atoms in the plasma increases by approximately a factor of 3 while the concentration of C containing molecules and molecular fragments decreases by approximately a factor of 2 to 3 depending on the species. The gas temperature does not rise significantly. Thus, increasing the H₂-to-CH₄ ratio by an order of magnitude also increases the flux of H atoms to C-containing molecules impinging on the substrate by approximately an order of magnitude. We use this information to help interpret the observed changes in the catalyst and CNT structure.

B. CNT structure

A broad range of CNT structures and sizes were observed with TEM, scanning electron microscopy (SEM), and

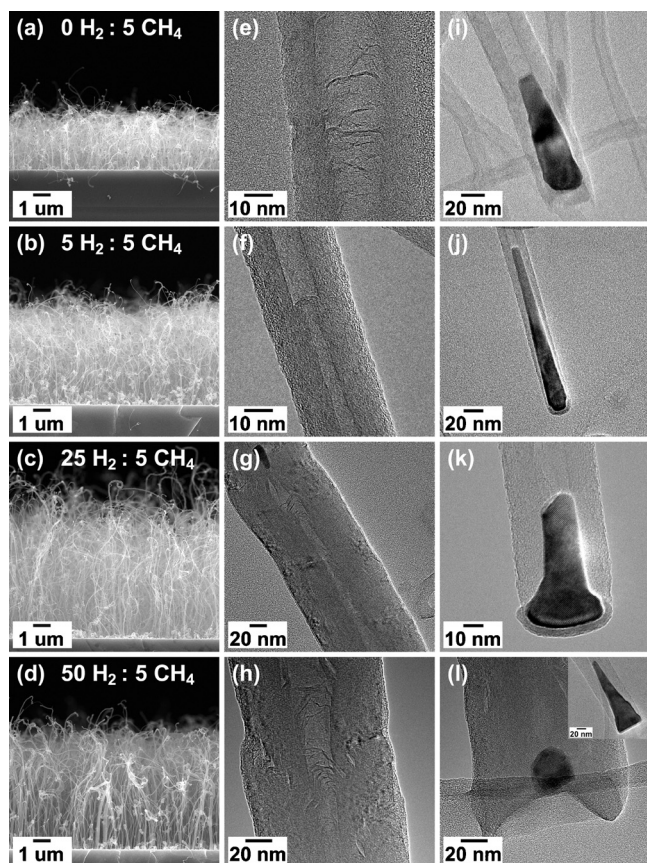


FIG. 4. (a)–(d) in the first column show cross-section SEM images of MWCNT films grown by catalytic PECVD using a 10 nm iron catalyst layer. H_2 -to- CH_4 flow rate ratio increases from top to bottom, and is indicated on each image. (e)–(h) in the second column show representative BF-TEM images of the most commonly-observed CNT structures for each experiment in the first column. (i)–(l) in the third column show representative BF-TEM images of the most abundant catalyst crystal morphology observed inside the bases of the MWCNTs shown in the corresponding (same row) first and second columns. The MWCNTs were deposited with feed gas that contained (a, e, i) 0 SCCM H_2 and 50 SCCM CH_4 , (b, f, j) 5 SCCM H_2 and 5 SCCM CH_4 , (c, g, k) 25 SCCM H_2 and 5 SCCM CH_4 , (d, h, l) 50 SCCM H_2 and 5 SCCM CH_4 .

Raman spectroscopy as the H_2 -to- CH_4 ratio in the feed gas was varied. The left column of SEM images in Fig. 4 shows the cross-sectional views of CNT films grown under different H_2 -to- CH_4 ratios. SEM images show the relatively dense films of CNT structures that grow normal to the substrate at all but the very highest hydrogen dilution, H_2 -to- CH_4 ratio of 20 (100 SCCM H_2). CNTs were not produced at an H_2 -to- CH_4 ratio of 20, and thus images from this experiment are not included in Fig. 4. Next to each SEM image, in the second column, is a bright field (BF) HR-TEM image that shows the representative CNT structure produced in each experiment. SEM and TEM analysis revealed that as the fraction of hydrogen was changed, the average CNT length, as well as both the average diameter and diameter distribution of the CNTs changed. Nanotubes grew to lengths ranging from 3.3–7 μm , depending on the H_2 -to- CH_4 ratio, after 30 min of plasma deposition. The shortest nanotubes were produced with no added hydrogen. Figure 5 shows the average length, and diameter, with standard deviations, of CNTs from each experiment, as measured from HR-TEM images.

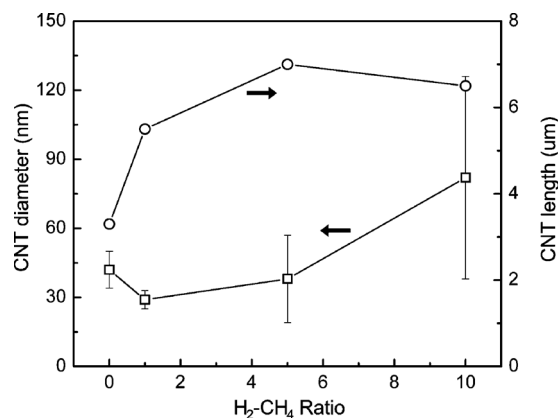


FIG. 5. Average CNT diameter (\square), and CNT length (\circ) as a function of H_2 -to- CH_4 flow rate ratio. Error bars are the standard deviation for each sample and is a measure of the diameter distribution.

Equal parts hydrogen and methane produced CNTs with the smallest average diameter, 29 nm, and narrowest diameter distribution. As the H_2 -to- CH_4 ratio was increased above one, the average diameter and diameter distribution increased significantly.

A methane plasma, with no added H_2 , produced CNTs with an average diameter of 42 nm [Figs. 4(a), 4(e), and 4(i)]. Most tubes exhibited frequent cupping along their length, i.e., interior walls would connect to form cups perpendicular to the nanotube axis, as shown in Fig. 4(e). Cups are formed when the hemispherical cap that forms and covers the tip of the catalyst (sometimes multiple layers) lifts off from the catalyst tip, and remains as a cup inside the CNT. Dangling graphene walls that neither formed full cups nor continuous walls were observed frequently on the interior of these tubes. Tube walls were found to extend beyond the catalyst crystal located at the base of the nanotube [Fig. 4(i)], indicating that the catalyst was lifted a few nanometers off the substrate during growth.

Equal parts H_2 and CH_4 produced the most well-graphitized tubes [Figs. 4(b), 4(f), and 4(j)], which were also the thinnest nanotubes with a very narrow diameter distribution (29 ± 5 nm). While occasional cupping was observed, all walls, both interior and exterior, were continuous, intact, and approximately constant diameter the entire length of the nanotube in most tubes.

At five times the amount of H_2 relative to CH_4 , a much wider variety of structures and sizes of tubes were produced [Figs. 4(c), 4(g), and 4(k)]. The most abundant nanotubes were ~ 40 nm in diameter; however, a number of tubes with diameters close to ~ 100 nm were also present. Those with diameters ~ 40 nm were of similar quality as those grown with no added H_2 and resembled the tube shown in Fig. 4(e). The large diameter tubes, however, were highly defective, and consisted of very thick walls, i.e., large number of walls [Fig. 4(g)]. The interior diameter was typically 1/9 the exterior diameter (compared to 1/3 for the smaller diameter tubes produced in all experiments), and contained numerous deformed cupped graphene layers, as well as sections of kinked walls. The walls of highly-defective tubes exhibited numerous kinks and curves and did not run exclusively parallel to the nanotube axis. The spacing between layers was also not

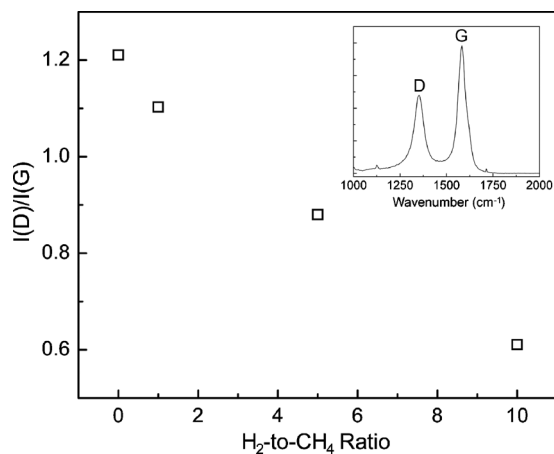


FIG. 6. Raman spectra (inset) from a MWCNT film. The ratio of the D and G peak intensities, $I(D)/I(G)$, as a function of H_2 -to- CH_4 flow rate ratio.

constant, due to these numerous kinks and curves. We presume that there are a large number of 5- and 7-member rings (defects) in the nanotube walls.

Further increase in the H_2 -to- CH_4 ratio, to 10, yielded many more large-diameter CNTs [Figs. 4(d), 4(h), and 4(l)]. CNTs with diameters ~ 100 nm or larger were now the most abundant type. All tubes, including the smaller-diameter tubes were very defective, exhibiting kinks, cups, and deformed interior graphene layers [Fig. 4(h)]. Most graphene walls were not parallel to the tube axis, but rather at a variety of angles, up to $\sim 45^\circ$. When the H_2 flow was increased to 100 SCCM, no significant nanotube growth was observed. TEM analysis revealed that some catalysts produced fat and deformed CNF-like structures, without an open interior and many catalysts were merely encapsulated with graphene shells.

Raman spectroscopy captured a clear change in the average CNT structure as a function of H_2 -to- CH_4 ratio in the feed gas mixture. The inset in Fig. 6 shows a typical Raman spectrum obtained from a CNT film which shows two major peaks, a G peak at ~ 1580 cm^{-1} , and a D peak at ~ 1350 cm^{-1} . The ratio of peak intensities, $I(D)/I(G)$, is often used as a measure of a carbon materials structure, and crystalline quality.^{26,27} The G peak corresponds to the in-plane stretching of sp^2 C–C bonds in rings or chains, while the D peak corresponds to breathing modes of sp^2 C–C bonds in rings.²⁷ The ratio $I(D)/I(G)$ for CNTs grown in our experiments is plotted as a function of H_2 -to- CH_4 ratio in Fig. 6. A dramatic decrease in this ratio is observed as the fraction of H_2 in the feed gas is increased. This decrease in $I(D)$ indicates increased disorder within the graphite (CNT wall) structure.²⁷ Specifically, this disorder may be manifested as a decrease in the average in-plane graphite cluster size,²⁸ or as other structural disorder that breaks the graphite structure symmetry. This would suggest that increasing H_2 produces CNTs whose walls more resemble bulk graphite, with relatively long-range order and few structural defects. Certain defects that may be present in the CNT walls would not necessarily be detectable using only TEM characterization. Alternatively, the observed decrease in $I(D)/I(G)$ may

be a measure of the amount of amorphous carbons present. Since a relatively large film area, ~ 1 μm was probed in a Raman measurement, the averaged Raman signal contains information from all carbons present, which may include amorphous carbons in addition to the graphite-like CNT structures. Thus, in this interpretation, increasing hydrogen concentration decreases the amount of amorphous carbon deposited.

C. Catalyst morphology and crystalline phase

Careful examination of the changes in the catalyst nanoparticle sizes and morphologies as a function of the H_2 -to- CH_4 ratio suggests that one mechanism by which hydrogen affects CNT structure is through its effect on the catalyst nanoparticles. Indeed, it appears that the wide range of CNT sizes and structures observed in these experiments is a direct result of the range of sizes, morphologies, and crystal structures of the catalyst crystals from which these nanotubes grow. Figure 4 (right column) and Fig. 7 show a collection of representative bright-field-transmission electron microscopy (BF-TEM) images of catalyst nanocrystals observed inside the base of MWCNTs. A clear change in both the size and shape of the catalyst crystals is evident as the amount of H_2 in the feed gas is increased.

The majority of CNTs grown from methane plasma, without H_2 , grew from slightly elongated oval-shaped catalyst crystals, approximately 100 nm in length, which exhibited rough and deformed faces [Figs. 4(i), 7(a), and 7(b)]. The highly disordered interior structure of the CNTs that grew from these catalysts, as described previously, is likely due to the rough and irregular catalyst edges. However, since the overall catalyst size is consistent, the resulting CNT diameter distribution is still narrow.

Addition of a small amount of H_2 (equal to methane flow) drastically improved the shape of the catalysts. Elongated tear-drop shaped catalysts with a constant smooth taper and lengths greater than 150–200 nm were commonly observed inside the base of the MWCNTs [Figs. 4(j), 7(d), and 7(e)]. The interfaces between the catalyst particles and the nanotube walls appeared very smooth, while the bases exhibited clear faceting. Production of well-graphitized CNTs with a very narrow diameter distribution was due to the similarity of all catalysts in this sample.

With five times more H_2 than CH_4 , a considerable change in catalyst shape was observed. Figures 4(k) and 7(g) show that the catalysts found inside the base of the most abundant CNTs, with diameters ~ 40 – 45 nm, were much shorter than those observed in experiments conducted with no or little H_2 . These catalysts consisted of a 30–40 nm long cylindrical region of approximately constant diameter, followed by a region at the base which flares outwards to define the exterior diameter of the CNT. During growth, the cylindrical portion of the catalyst often became detached from the flared base region. This is evident by the high number of cylindrical catalysts observed ~ 5 – 10 nm up inside the base of the nanotube, as shown in the inset of Fig. 7(g). Although not nearly as abundant, a second, much larger catalyst type

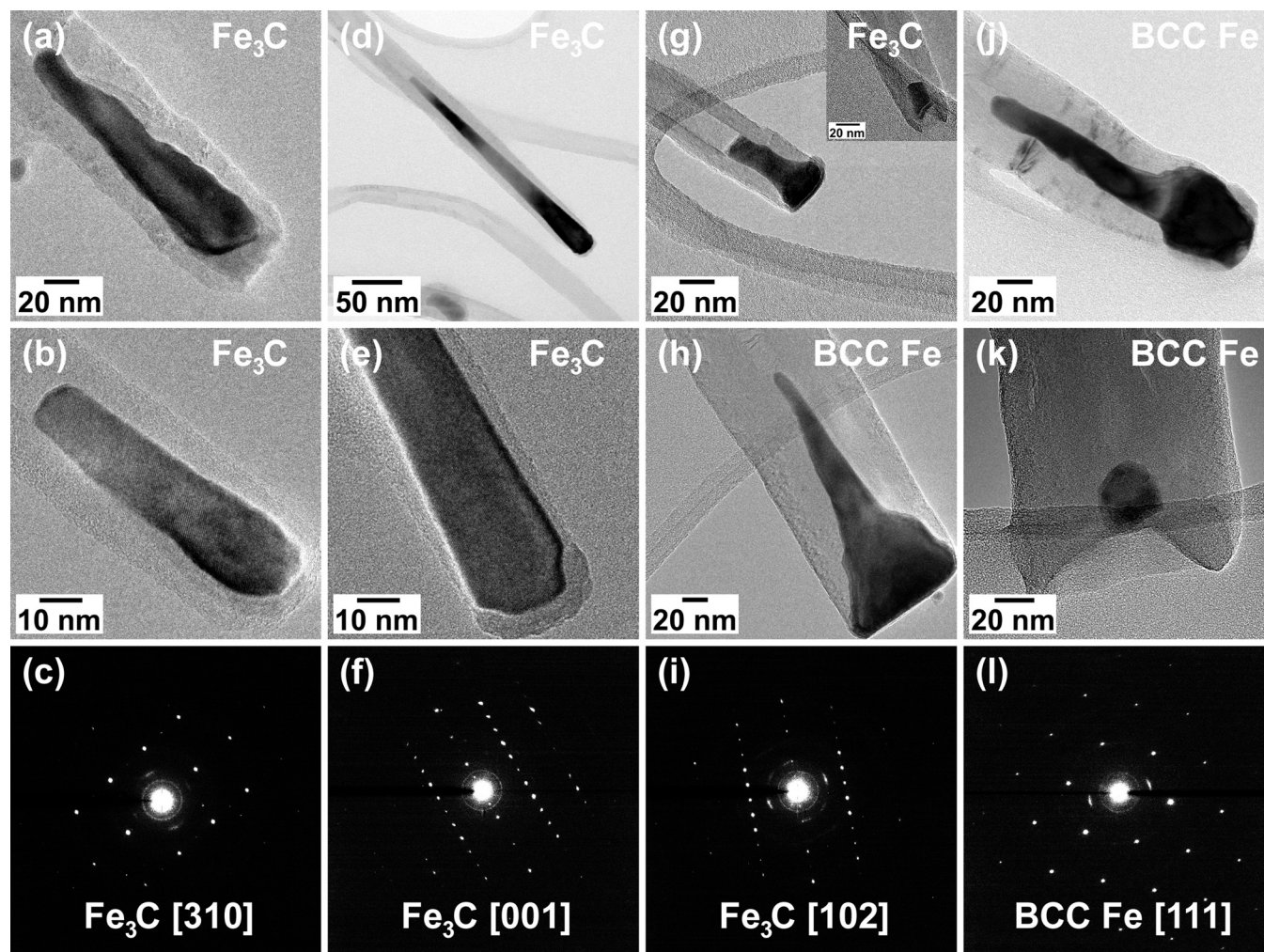


FIG. 7. BF-TEM images of (top two rows), and SAED patterns (bottom row) from the most abundant catalyst crystals observed inside the base of MWCNTs grown using H_2 -to- CH_4 flow rate ratios of (SCCM H_2 : SCCM CH_4) (a)–(c) 0:5, (d)–(f) 5:5, (g)–(i) 25:5, and (j)–(l) 50:5 SCCM.

was observed inside the base of nanotubes with diameters ~ 90 – 100 nm [Fig. 7(h)]. Consisting of a perfectly flat base, this cone-shaped catalyst exhibited numerous step-edges as it extended up into the CNT.

A H_2 flow of 50 SCCM, ten times the methane flow rate, was the highest hydrogen fraction found to produce CNTs. The widest range of catalyst morphologies and sizes was also observed under these conditions. All catalysts examined in CNTs grown with a H_2 -to- CH_4 ratio of 10 appeared highly deformed. In addition to the conical-shaped catalysts inside CNTs with diameters ~ 90 – 100 nm [Fig. 4(l) inset], as observed in the previous experiment, multiple other morphologies were present. Tadpole-shaped catalysts were often observed inside nanotubes with diameters ~ 50 – 60 nm, as shown in Fig. 7(j). Inside the base of the CNTs with diameters over 100 nm, catalysts appeared roughly spherical, yet much smaller (typically ~ 25 nm) than the nanotube diameter [Figs. 4(l) and 7(k)]. Most of these larger nanotubes, however, were open at their base, suggesting that during removal by sonication from the substrate, tubes were separated from their catalysts.

In addition to affecting catalyst morphology, hydrogen controls the crystalline phase of the catalysts. Using CBED pattern analysis combined with crystal tilting, the crystalline

phase of the most abundant catalyst crystals at the base of CNTs from each experiment was determined. From each sample, 12 to 22 crystals were individually tilted, using a double-tilt holder inside the TEM, to multiple connected zone axes (not shown). The symmetry of each zone axis combined with the angular relationships between pairs of zone axes uniquely define the crystal system.²⁹ Examples of single-crystal electron diffraction patterns obtained from the most abundant catalyst phase from each experiment are shown in Figs. 7(c), 7(f), 7(i), and 7(l). Although each catalyst is single crystalline, they exhibit combinations of small-angle ($\sim 1^\circ$ – 3°) rotations, twists, and bends along their axial length between adjacent locations, as reported elsewhere.³⁰ The most abundant catalysts inside the base of CNTs grown with 0, 5, and 25 SCCM H_2 flows were found to be of the Fe_3C (cementite) crystal phase (orthorhombic space group $Pnma$ no. 62, $a=0.5008$ nm, $b=0.4465$ nm, $c=0.6725$ nm). However, the larger catalysts that produced tubes with diameters ~ 90 – 100 nm with 25 SCCM H_2 were found to be body-centered cubic (bcc) iron (cubic space group $I23$ no. 197, $a=0.287$ nm). Similarly, at 50 SCCM, the catalysts producing the abundant large diameter tubes were also determined to be bcc iron.

IV. DISCUSSION

The observations above suggest that the H₂-to-CH₄ ratio in the feed gas determines the relative fluxes of atomic H- and C-containing-species impinging on the catalyst. We will refer to this ratio as the H-to-C ratio for simplicity even though C may be brought to the catalyst in a variety of molecular fragments. The ratio of H-to-C flux in turn determines the CNT structure through the catalysts morphology and phase. For example, the H-to-C flux determines the phase of the catalyst particle. When H concentration in the plasma is low compared to C containing species, Fe catalyst particles are quickly converted into Fe₃C as C containing species adsorb and react on the Fe surface. In contrast, it appears that under strongly reducing environments, i.e., when H atom concentration is increased, Fe₃C is unable to form, and hence the nanotubes grow from bcc iron catalyst nanocrystals. It appears that in presence of high H concentrations, CH_x fragments adsorbing on the surface could easily be converted back to volatile methane and desorbed from the surface before they have a chance to convert the iron particle into carbide. Indeed, when H₂-to-CH₄ ratio was increased to five, a small number of bcc catalyst crystals were observed. At even higher H₂-to-CH₄ ratios and correspondingly high hydrogen concentrations, the majority of nanotubes grew from bcc iron catalyst nanocrystals. These findings may help explain why CNTs have been observed growing from a variety of iron-based catalysts. It is possible that differences in absolute atomic hydrogen concentration in different reactors or under different plasma operating conditions may help account for the variety of reported catalyst phases and morphologies found inside MWCNTs.^{14–18}

Elongated Fe₃C catalyst crystals that produce relatively thin, well-graphitized CNTs are formed when the H₂-to-CH₄ ratio in the feed gas is approximately one. However, when the catalyst shape is tapered and the widths of the tip and the base are disparate, many walls form and emanate from the edges of the catalyst particles. It seems that this situation leads to thick CNT walls with very small ratio of the inner diameter to the outer diameter. Moreover, severely tapered catalyst shapes are most common when the catalyst is bcc iron. This difference is likely due to the differences in the mechanical properties of Fe₃C and bcc iron. bcc Fe plastically deforms and yields much easier than Fe₃C: Yield strengths of bcc Fe and Fe₃C are ~140 MPa and ~5 GPa, respectively. The catalyst experiences very large compressive stresses during growth, which would squeeze and taper the catalyst nanoparticle. Moreover, a positive feedback loop is set up during initial stages of growth wherein tapering the nanocrystal leads to formation of additional CNT walls which in turn increases the compressive stress and causes more taper which leads to more walls.

It is interesting to note that we observe only the cementite phase even though there are a number of other iron carbide phases, including the hexagonal, Hagg, Eckstrom and Adcock, and Pomey phases. However, we have observed some diffraction patterns that we were unable to assign to a specific phase. When the catalyst particle is iron, we primarily observe the bcc phase. However, we have also observed

a few cases where CNTs grew from fcc iron. Observation of fcc iron is unexpected at ambient conditions. There is a volume expansion of 8.1% associated with the fcc to bcc transformation, and it is thought that the surrounding graphene walls may prevent this transformation. Thus, we presume that if fcc is present during growth at high temperature, the pressure from the surrounding CNT walls should keep the phase as fcc. Iron can also exist in the hexagonal-close-packed ϵ phase at high pressure. Again, however, there is a significant volume expansion of ~20% associated with the hcp to bcc transformation. We do not observe the hcp phase.

V. CONCLUSIONS

The relation among gas phase composition, catalyst structure and morphology, and CNT structure during PECVD of CNTs, was studied using a combination of material and gas-phase characterization techniques. Optical emission and IR absorption spectroscopy revealed that addition of H₂ to a CH₄/Ar plasma resulted in a decrease in the concentration of reactive carbon-containing species, specifically CH, C₂, and C₂H₂, but an increase in atomic hydrogen concentration. As the amount of hydrogen was increased, the average diameter, diameter distribution, and CNT structure changed, because the size, shape, and phase of the catalyst crystals changed. At H₂-to-CH₄ ratios of 0, 1, and 5, CNTs grew from Fe₃C catalyst nanocrystals. Equal parts H₂ and CH₄ produced CNTs of the highest quality and uniformity. As H₂ was increased further, CNTs no longer grew from Fe₃C catalysts, but rather from bcc iron catalyst nanoparticles. Severe deformation of ductile iron nanocrystals leads to the formation of a tapered catalyst shape, which in turn produces CNTs with many walls and a very small inner diameter to outer diameter ratio.

ACKNOWLEDGMENTS

The authors thank Dr. O. Ugurlu for technical support. This material is based upon work supported by the National Science Foundation (NSF) under Grant No. CBET-0613629. Part of this work was carried out in the Institute of Technology Characterization Facility, University of Minnesota, which has received capital equipment funding from the NSF through the MRSEC, ERC, and MRI programs.

APPENDIX

1. GAS TEMPERATURE MEASUREMENTS

FTIR spectroscopy was used to measure the gas temperature in the plasma during CNT growth assuming that the translational, vibrational, rotational degrees of freedom are all equilibrated. This is an excellent assumption under the relatively high pressure of 10 torr used for nanotube growth. Thus the gas temperature can be measured by extracting the rotational temperature from a rotational-vibrational absorption band of methane.

The rotational-vibrational absorption band of methane at 3017 cm⁻¹ shown in Fig. 2(a) consists of three branches, labeled P, Q, and R. The series of peaks that make up the P and R branches are due to transitions between rotational energy levels, each corresponding to a different value of angu-

lar momentum.³¹ The angular quantum numbers associated with the first few peaks of the R branch are indicated in Fig. 2(a). The intensity of each rotational line is proportional to the fraction of molecules that were initially in that particular rotational energy level.³² At equilibrium, Boltzmann statistics describe the relative populations of rotational levels, and the intensity distribution among rotational levels in the R branch can be used to determine the rotational temperature. The number of molecules in the J th energy level, N_J , relative to the number in the ground state, N_0 , for CH₄ is given by

$$\frac{A_J}{A_0} = \frac{N_J}{N_0} = \frac{4}{3(2J+1)^2} \exp\left(-\frac{BJ(J+1)}{kT}\right), \quad (1)$$

where J is the angular momentum quantum number, A_J and A_0 are the absorption intensities of the J th and ground state energy level peaks, respectively, B is the rotational constant of the molecule, k is the Boltzmann constant, and T is the absolute temperature.^{32,33} A plot of $J(J+1)$ versus $\ln[A_J/(A_0\{4/[3(2J+1)^2]\})]$ yielded a straight line with slope equal to B/kT , as shown in Fig. 2(b). The rotational constant of methane was calculated from absorption measurements with no plasma activation with known gas temperature of 300 K to be 6.33 cm⁻¹. This value was then used in calculating the gas temperature while plasma was turned on. Gas temperatures calculated with this method ranged from 300 to 345 K.

2. CH₄ DISSOCIATION MEASUREMENTS

The fraction of methane molecules dissociated in the plasma to form other reactive species was calculated by measuring the change in the magnitude of methane absorption upon igniting the plasma. Figure 2(a) shows the two overlaid absorbance spectra obtained with plasma off (black) and on (red). Absorbance, or optical density of the methane gas, A , is related logarithmically to the fraction, I , of incident light, I_0 , that passes through the gas in the chamber by $A = -\log(I/I_0)$. The absorbance, A is also related to the concentration of absorbing species, N (cm⁻³), their absorption cross-section, σ (cm⁻²), and the path length that the light travels through the absorbing medium by $A = \sigma nl$. Since the density of methane gas in the reaction chamber is known (partial pressure of CH₄ is calculated from gas flows and total pressure), an absorbance measurement without plasma activation yielded both the integrated and average methane absorption cross-sections across the band centered at 3017 cm⁻¹. Specifically, an integrated absorption cross-section across the band, $\int_{\tilde{\nu}_1}^{\tilde{\nu}_2} \sigma(\tilde{\nu}) d\tilde{\nu}$, was calculated to be 6.18×10^{17} cm by integrating the measured absorbance across the entire absorp-

tion band, from 3001.2–3178.8 cm⁻¹. While the average absorption cross-section across the band, $\int_{\tilde{\nu}_1}^{\tilde{\nu}_2} \sigma(\tilde{\nu}) d\tilde{\nu} / \int_{\tilde{\nu}_1}^{\tilde{\nu}_2} d\tilde{\nu}$, was calculated to be 3.48×10^{19} cm².

- ¹R. H. Baughman, A. A. Zakhidov, and W. A. de Heer, *Science* **297**, 787 (2002).
- ²A. Jorio, *Carbon Nanotubes: Advanced Topics in the Synthesis, Structure, Properties, and Applications* (Springer, Berlin, 2008).
- ³M. S. Dresselhaus, G. Dresselhaus, J. C. Charlier, and E. Hernandez, *Philos. Trans. R. Soc. London, Ser. A* **362**, 2065 (2004).
- ⁴M. Meyyappan, *J. Phys. D: Appl. Phys.* **42**, 213001 (2009).
- ⁵M. S. Bell, K. B. K. Teo, and W. I. Milne, *J. Phys. D: Appl. Phys.* **40**, 2285 (2007).
- ⁶J. B. O. Caughman, L. R. Baylor, M. A. Guillorn, V. I. Merkulov, D. H. Lowndes, and L. F. Allard, *Appl. Phys. Lett.* **83**, 1207 (2003).
- ⁷T. Y. Lee, J. H. Han, S. H. Choi, J. B. Yoo, C. Y. Park, T. Jung, S. Yu, W. K. Yi, I. T. Han, and J. M. Kim, *Diamond Relat. Mater.* **12**, 851 (2003).
- ⁸P. E. Nolan, D. C. Lynch, and A. H. Cutler, *J. Phys. Chem. B* **102**, 4165 (1998).
- ⁹M. Chhowalla, K. B. K. Teo, C. Ducati, N. L. Rupesinghe, G. A. J. Amaratunga, A. C. Ferrari, D. Roy, J. Robertson, and W. I. Milne, *J. Appl. Phys.* **90**, 5308 (2001).
- ¹⁰Y. S. Woo, D. Y. Jeon, I. T. Han, N. S. Lee, J. E. Jung, and J. M. Kim, *Diamond Relat. Mater.* **11**, 59 (2002).
- ¹¹S. H. Lim, H. S. Yoon, J. H. Moon, K. C. Park, and J. Jang, *Appl. Phys. Lett.* **88**, 033114 (2006).
- ¹²L. Delzeit, I. McAninch, B. A. Cruden, D. Hash, B. Chen, J. Han, and M. Meyyappan, *J. Appl. Phys.* **91**, 6027 (2002).
- ¹³N. M. Rodriguez, A. Chambers, and R. T. K. Baker, *Langmuir* **11**, 3862 (1995).
- ¹⁴H. Kim and W. Sigmund, *Carbon* **43**, 1743 (2005).
- ¹⁵Y. Yao, L. K. L. Falk, R. E. Morjan, O. A. Nerushev, and E. E. B. Campbell, *J. Mater. Sci.: Mater. Electron.* **15**, 583 (2004).
- ¹⁶D. Golberg, M. Mitome, C. Muller, C. Tang, A. Leonhardt, and Y. Bando, *Acta Mater.* **54**, 2567 (2006).
- ¹⁷H. Yoshida, S. Takeda, T. Uchiyama, H. Kohno, and Y. Homma, *Nano Lett.* **8**, 2082 (2008).
- ¹⁸V. D. Blank, Y. L. Alshevskiy, A. I. Zaitsev, N. V. Kazennov, I. A. Perezhogin, and B. A. Kulnitskiy, *Scr. Mater.* **55**, 1035 (2006).
- ¹⁹A. Tanaka, S. H. Yoon, and I. Mochida, *Carbon* **42**, 591 (2004).
- ²⁰S. Agarwal, A. Takano, M. C. M. van de Sanden, D. Maroudas, and E. S. Aydil, *J. Chem. Phys.* **117**, 10805 (2002).
- ²¹J. W. Coburn and M. Chen, *J. Appl. Phys.* **51**, 3134 (1980).
- ²²A. Gicquel, M. Chenevier, K. Hassouni, A. Tserepi, and M. Dubus, *J. Appl. Phys.* **83**, 7504 (1998).
- ²³I. B. Denysenko, S. Xu, J. D. Long, P. P. Rutkevych, N. A. Azarenkov, and K. Ostrikov, *J. Appl. Phys.* **95**, 2713 (2004).
- ²⁴J. Ma, M. N. R. Ashfold, and Y. A. Mankelevich, *J. Appl. Phys.* **105**, 043302 (2009).
- ²⁵C. Deschenaux, A. Affolter, D. Magni, C. Hollenstein, and P. Fayet, *J. Phys. D: Appl. Phys.* **32**, 1876 (1999).
- ²⁶R. J. Nemanich, J. T. Glass, G. Lucovsky, and R. E. Shroder, *J. Vac. Sci. Technol. A* **6**, 1783 (1988).
- ²⁷A. C. Ferrari and J. Robertson, *Phys. Rev. B* **61**, 14095 (2000).
- ²⁸F. Tuinstra and J. L. Koenig, *J. Chem. Phys.* **53**, 1126 (1970).
- ²⁹D. B. Williams and C. B. Carter, *Transmission Electron Microscopy: A Textbook for Materials Science* (Plenum, New York, 1996).
- ³⁰M. J. Behr, K. A. Mkhoyan, and E. S. Aydil, *Carbon* **48**, 3840 (2010).
- ³¹G. Herzberg, *Molecular Spectra and Molecular Structure* (Prentice-Hall, New York, 1939).
- ³²D. A. McQuarrie, *Quantum chemistry* (University Science Books, Sausalito, California, 2008).
- ³³R. S. McDowell, *J. Quant. Spectrosc. Radiat. Transf.* **38**, 337 (1987).